*Korean J. Chem. Eng.*, 39(6), 1632-1640 (2022)
DOI: 10.1007/s11814-021-1037-4

pISSN: 0256-1115
eISSN: 1975-7220

# Fabrication of Ag-doped ZnO/PAN composite nanofibers by electrospinning: Photocatalytic and antiviral activities

**Jinsoo Yoon*, Joohyun Kim**, Soomin Park***, Yong Won Jeong***, Changha Lee**, and Seong-Geun Oh*,†**

*Department of Chemical Engineering, Hanyang University, Seoul 04763, Korea
**School of Chemical Engineering, Institute of Chemical Process (ICP), Institute of Engineering Research, Seoul National University, Seoul 08826, Korea
***Sensor Lab, Smart Device Team, Samsung Research, Samsung Electronics Co., Ltd., Seoul 06756, Korea
(*Received 19 July 2021 • Revised 19 November 2021 • Accepted 2 December 2021*)

**Abstract**−Ag-doped ZnO nanoparticles (AZNs) were directly synthesized using sol-gel method to embed into polyacrylonitrile (PAN) nanofibers by electrospinning. The synthesized AZNs were optically and structurally characterized by UV-VIS spectroscopy, photoluminescence spectroscopy, high resolution HR-TEM and XRD. The photocatalytic activity of the AZNs was examined by photocatalytic degradation of methylene blue to correlate with their antiviral efficacy in PAN nanofibers fabricated via electrospinning technique. The PAN nanofibers containing AZNs were characterized using SEM and EDS. Finally, antiviral activity of AZNs/PAN nanofibers was investigated by using virus $\phi$x174 under visible light irradiation. As a result, the antiviral efficacy of nanofibers increased as the concentration of Ag in AZNs increased. The results show that better antiviral efficacy was obtained in AZNs/PAN nanofibers prepared with AZNs of higher photocatalytic performance.

Keywords: Ag-doped ZnO Nanoparticles, Photocatalytic Activity, Antiviral Efficacy, Nanofibers, Electrospinning

## INTRODUCTION

Throughout history, there have been numerous pandemic diseases, such as SARS [1], H1N1 influenza viruses [2] and COVID-19 [3], which have threatened both human health and economic development. These viruses are rapidly transmitted among individuals by direct person-to-person contact and indirect pathways. Studies have shown that one of the main indirect pathways of pandemic disease is the aerosols made of virus-laden droplets [4]. Therefore, materials that deactivate viruses have been extensively studied in the era of the pandemic. Hydrogen peroxide [5] and alcohols [6] in common sanitizer serve as an antiviral agent to denature protein in virus [7]. However, these substances are not suitable to fabricate filters and masks to protect against spreading virus due to their rapid evaporation. Consequently, solid-state antiviral metal is more feasible and useful for preventing from surface contamination by bacteria and virus.

Photocatalysis has been studied to explore for antiviral and antimicrobial activity. In particular, photocatalysts of solid semiconducting metal oxides have attracted intense attention for use in a wide variety of applications including self-cleaning [8], removal of pollutant [9], antibacterial [10] and antivirus activity [11]. Among semiconducting metal oxides, $TiO_2$ and ZnO are widely used due to their effective photocatalytic activity, being inexpensive and eco-friendly [12,13]. Among these materials, ZnO shows outstanding biocompatibility. Zinc is an essential trace element known to be widely present in all body tissues including brain, muscles, bones and skin. Thus, ZnO with good biocompatibility and relatively low toxicity has excellent biomedical applications, such as wound healing, anticancer, drug delivery and antibacterial treatment [14,15]. However, wide band gap and fast rate of recombination of electrons and holes becomes a limitation to their usage in practical applications. Their wide band gap allows to absorb only UV region light, and the fast recombination rate results in low efficiency on converting photons to electrons [16,17]. Typical ZnO nanoparticle has a band gap of 3.37 eV and an excitation binding energy of 60 meV [18], which is able to absorb visible region light. Surface area and defect of nanoparticles play an important role in determining the bandgap of semiconductors [19]. The studies about doping of ZnO with transition metals to lead surface defect have been reported often. These transition metals such as Co [20], Cd [21], Cu [22] and Ag [23] eventually narrow the band gap of semiconductor to enhance optical absorption. Furthermore, the use of dopants to improve multiple properties of ZnO from antimicrobial, electrical, piezoelectric to magnetic has been reported in several studies [24, 25]. Especially, Ag has been studied to impart properties which inhibit virus among dopants [26].

Electrospinning method is the one of promising methods for fabricating organic and inorganic nanofibers. This method provides a simple and cost-effective process to produce continuous and homogeneous nanofiber of submicron diameter [27]. In the process, high voltage electric field is applied to the solution in syringe to form a jet from nozzle. The jet becomes nanofibers with uniform diameter during drying and deposits on the collector [28]. The morphology and diameter of the synthesized diameter depends on the rheological property of polymeric solutions, distance between noz-

†To whom correspondence should be addressed.
E-mail: seongoh@hanyang.ac.kr
Copyright by The Korean Institute of Chemical Engineers.

zle and collector, and strength of the applied electric field [29]. Various polymers have been employed in electrospinning method to fabricate ultrafine fibers in recent years. PAN is one of the polymers widely used for electrospinning due to its high mechanical strength, chemical stability and non-toxicity [30,31].

In this study, Ag-doped ZnO nanoparticles (AZNs) with different amounts of Ag were prepared using sol-gel method and characterized structurally and optically. The photocatalytic property of synthesized AZNs was evaluated by using methylene blue (MB) in water under UV and visible light irradiation. Then, Ag doped ZnO/PAN nanofibers were prepared via electrospinning. The antiviral activity of electrospun fibers was investigated by inactivation of bacteriophage $\phi$x174. Finally, the relationship between photocatalytic activity of AZNs and antiviral efficacy of AZNs/PAN nanofibers was investigated.

## EXPERIMENTAL

### 1. Materials

Zinc acetate dehydrate (Zn $(CH_3COO)_2 \cdot 2H_2O$, Sigma-Aldrich), potassium hydroxide (KOH, JUNSEI), ethanol ($CH_2CH_2OH$, 99.9%, DAEJUNG), silver nitrate (ACS Reagent, 99+% Sigma-Aldrich) were used to synthesize AZNs using sol-gel method. Methylene blue (MB) was purchased from DAEJUNG Chemicals in Korea to examine photocatalytic activity of AZNs. PAN (polyacrylonitrile $M_w$=150,000) was purchased from Sigma-Aldrich to fabricate nanofibers.

### 2. Synthesis of Ag Doped ZnO Nanoparticles (AZNs)

AZNs were prepared through sol-gel method. Zinc acetate dehydrate (10 mmol) and 0, 2, 4 wt% of silver nitrate were dissolved in 100 ml of ethanol at 60 °C, respectively. KOH (20 mmol) dissolved in 50 ml of ethanol at 60 °C was added into Ag and Zn solution. The mixture was stirred for three hours, then the color changed from white to dark brown. The resultant solution remained at room temperature for several hours. The crude solution was centrifuged at 3,000 rpm for 15 minutes, and rinsed with ethanol for several times to remove residues and impurities. The obtained precipitates were dried in oven at 80 °C for 12 hr.

### 3. Characterization of AZNs

The morphological and structural properties of AZNs were investigated using high resolution electron microscopy (HR-TEM, JEOL TEM-3010) and X-ray diffractometry (XRD, Rigaku, minFlex600). The optical properties of AZNs were analyzed using UV-Vis spectrometer (Agilent Technologies, Cary 8454) and photoluminescence spectrometer (PicoQuant, FlouTime 300). In addition, electron paramagnetic resonance analysis was performed with a JEOL JES-X310. The photoelectrochemical experiments were conducted using a potentiostat (VersaSTAT 3, Princeton Applied Research). ITO glass deposited with photocatalyst, Pt plate and Ag/AgCl electrode were used as the working electrode, counter electrode and reference electrode, respectively. Phosphate buffer solution (0.5 M) was used as the electrolyte and a Xenon lamp with 300 W was used as the light source.

### 4. Photocatalytic Activity Measurements

Photocatalytic performance of AZNs was investigated by measuring the degradation of MB under both UV and visible light irradiation. In the experiment, 0.05 g of AZNs was added to a 100 ml of aqueous 10 ppm MB solution for UV light exposure. In the case of visible light test, 0.1 g of AZNs was added to 100 ml of aqueous 5 ppm MB solution. UV light (400 W, UV-H-0.4, Korea) with a wavelength of 254 nm and Tungsten Halogen lamp (150 W) with a wavelength range of 400 to 2,200 nm as a visible light source were used for light irradiation. The distance between light source and the solution was 20 cm. Before the light exposure, the mixtures were sonicated for 30 min and stirred for 30 min under dark condition. During photocatalysis, the solution was stirred and 7.5 ml aliquot was extracted at a certain time interval; the collected aliquots were centrifuged to separate the particles. When aliquots were extracted, they did not return to original solution. The degraded MB concentration was measured by a UV-Vis spectrophotometer. The absorbance of suspension was measured at $\lambda_{max}$= 664 nm.

### 5. Preparation of Ag-doped ZnO/PAN Nanofibers

The AZNs (0.5 g) were re-dispersed in 4.5 g of N, N-dimethylformamide (DMF). In the meantime, 10 wt% PAN solution was prepared. Ag-doped ZnO colloid was added dropwise into the polymeric solution. The relative weight percentage of nanoparticle was fixed at 10% with respect to PAN. The nanofiber was collected using electrospinning method. The solution was pumped at the feed rate of 1.0 mL/h toward the collector. The distance between tip to collector was kept at 15 cm, and 15-20 kV of electric field was applied. The condition of the chamber was maintained with temperature at 25-28 °C. The fabricated nanofiber was dried for 1 h at 80 °C in vacuum oven.

### 6. Characterizations of AZNs/PAN Composite Nanofibers

The morphology of the fabricated nanofibers was investigated using transmission electron microscopy (TEM, JEOL JEM-2100), and field emission scanning electron microscope (FE-SEM, JEOL JSM-6700F). The chemical composition of electrospun nanofiber was analyzed using energy dispersive X-ray spectroscopy (EDS) equipped in FE-SEM.

### 7. Antiviral Activity Measurement

To evaluate virucidal activity during photocatalysis, *Phi X 174* (ATCC 13706-B1) bacteriophages and *Escherichia coli* (*E. coli*, ATCC 13706) were used as a model virus and its host organism, respectively. The *E. coli* host was cultivated in a Dicfo nutrient broth, and Phi X 174 bacteriophage was inoculated and incubated in the prepared *E. coli* solution for 18-24 h at 37 °C under vigorous shaking (120 rpm). The cultural solution was centrifuged at 3,000 rpm for 15 min, and the supernatant was separated to remove cell debris of the host bacteria. The population of Phi X 174 was determined by plaque assay method [32]. All experiments were performed using a rectangular reactor ($2 \times 2 \times 1$ $cm^3$) sterilized by autoclave at 121 °C for 15 min prior to use. The reactor was mounted on test jig equipped with LED bar (Blue LED, irradiating monochromatic light with a center wavelength of 470 nm). The 1 mL of virus solution containing $10^6$ PFU/mL was placed on the surface of prepared nanofibers. Then, microbial inactivation was initiated by irradiation of blue LED. The 0.1 mL of aliquots were collected at pre-determined times and immediately diluted with phosphate buffered solution (PBS, pH 7.2). The diluted aliquots were stored in dark prior to plaque assay to quench the reaction.

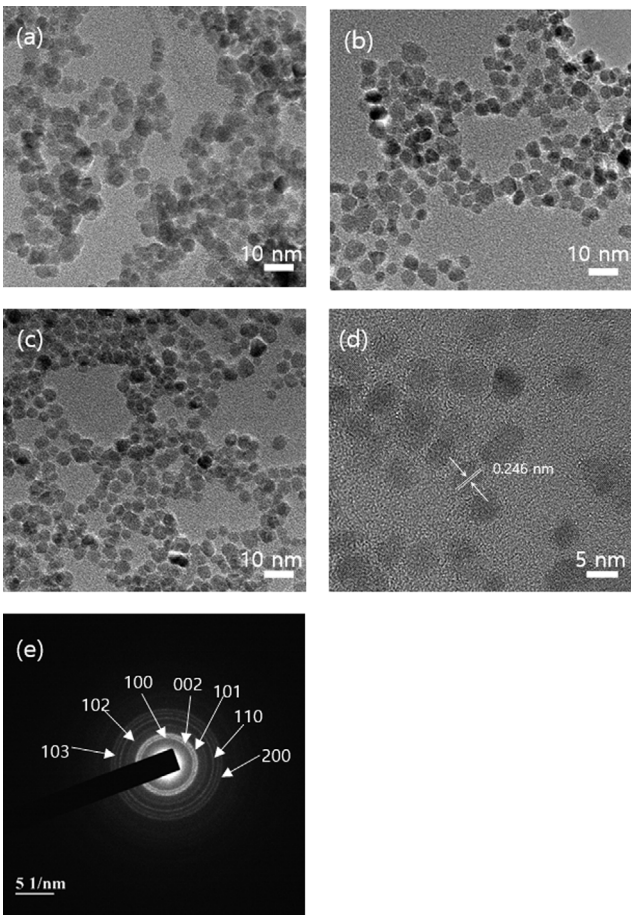


**Fig. 1. TEM images of synthesized (a) ZnO (b) Ag 2.0 ZnO and (c) Ag 4.0 ZnO (d) HR-TEM image of Ag 4.0 ZnO. Distance between ZnO lattice planes are denoted with white arrows and (e) SAED patterns of Ag 4.0 ZnO.**

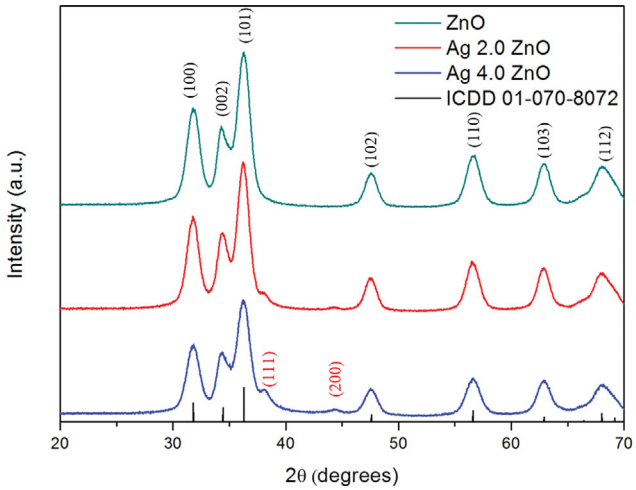


**Fig. 2. XRD patterns of synthesized ZnO, Ag 2.0 ZnO and Ag 4.0 ZnO.**

## RESULTS AND DISCUSSION

### 1. Characterization of AZNs

The AZNs synthesized with different amounts of $AgNO_3$ (0.0%, 2.0%, and 4.0 wt%) are abbreviated as ZnO, Ag 2.0 ZnO and Ag 4.0 ZnO, respectively. HR-TEM and TEM images in Fig. 1 show the morphological and structural properties of ZnO and AZNs. Fig. 1(a)-(c) indicate that ZnO, Ag 2.0 ZnO and Ag 4.0 ZnO have spherical shapes and average diameters of 9.31±1.45 nm, 9.85±1.78 nm and 10.22±1.71 nm, respectively. The spacing of lattice plane of 0.246 nm was observed, which corresponds to (101) plane of hexagonal Wurtzite structure of ZnO (Fig. 1(d)). Seven diffraction rings were observed in the SAED pattern (Fig. 1(e)). The seven rings correspond to the (100), (002), (101), (102), (110), (103) and (200) planes of the Wurtzite structure of ZnO. The crystallinity of synthesized nanoparticles was investigated using XRD. Most of XRD peaks shown in Fig. 2 are well matched with ZnO reference peaks reported in ICDD card (No. 01-070-8072). The major three peaks of Wurtzite ZnO were observed at 31.9°, 34.0° and 36.2°, which correspond to (100), (002) and (101) planes, respectively. Two additional peaks at 38° and 44° were detected for Ag-doped ZnO nanoparticles, which correspond to (111) and (200) planes in the face centered cubic phase of metallic Ag [33].

The optical properties of synthesized AZNs were investigated using UV-vis spectroscopy. Fig. 3(a) displays the UV-vis absorption spectra of ZnO and AZNs. The band gap energies ($E_g$) were

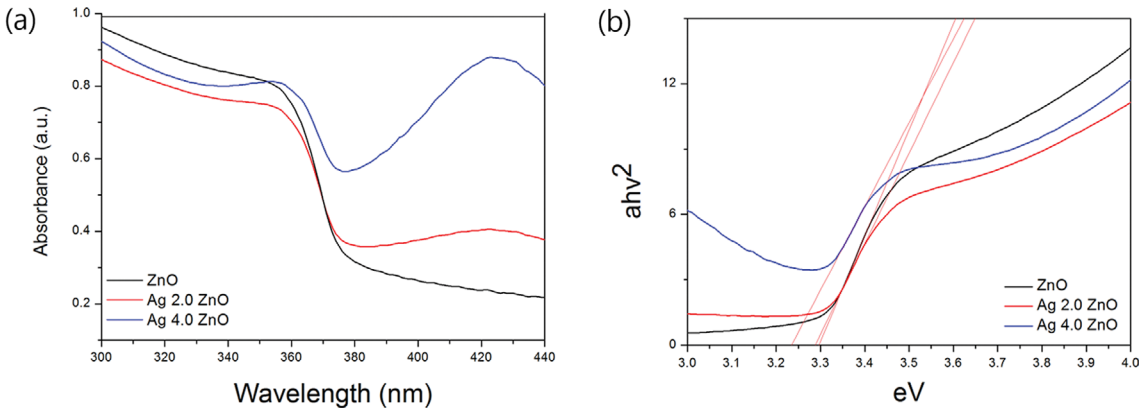


**Fig. 3. (a) UV-Vis adsorption spectra of ZnO, Ag 2.0 ZnO, and Ag 4.0 ZnO. (b) Tauc plot of ZnO, Ag 2.0 ZnO, and Ag 4.0 ZnO.**

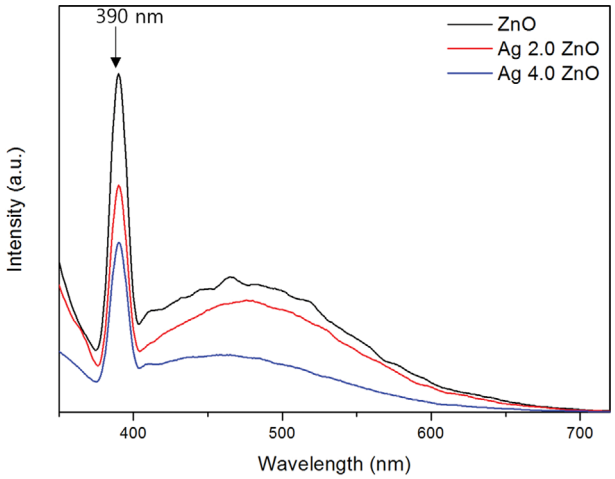


**Fig. 4. Photoluminescence spectra of ZnO, Ag 2.0 ZnO, and Ag 4.0 ZnO.**

calculated by using Tauc plot method described in Eq. (1) and plotted in Fig. 3(b).

$$\alpha h\nu = \beta(h\nu - E_g)^n \quad (1)$$

where $\alpha$ is the absorption coefficient, $\beta$ is the proportionality constant, hv is the photon energy and n is the transition index. The calculated band gap energies of ZnO, Ag 2.0 ZnO and Ag 4.0 ZnO were about 3.30 eV, 3.28 eV, and 3.23 eV, respectively. These results demonstrate that there is red shift of absorption edge and decrease in band gap energy as the concentration of Ag increases. This is due to the substitution of Zn with Ag in the ZnO lattice. Ag creates an intermediate energy state between valence band and conduction band of ZnO, and acts as photon acceptor altering the band gap of ZnO nanoparticles. As a result, the band gap of ZnO becomes narrow with the increased Ag content [34,35]. Fig. 4 describes the photoluminescence spectra of pristine ZnO and AZNs at room temperature. There are two peaks observed in the UV and visible regions. An intense peak located at around 390 nm indicates the near band edge emission which is related to the free excitonic recombination in ZnO. Another weak and broad emission band between 400 to 650 nm shows decreased intensity as the doping concentration of Ag increases. It can be inferred that the weak emission intensity is due to the substitution of Zn ion and interstitial forming by doping of Ag ions into ZnO nanostructure. Ag acts as good electron acceptor, and doping of Ag eventually leads to electron transfer from conduction band of ZnO to energy level of Ag. As a result, recombination of photogenerated electrons and holes becomes retarded, resulting in enhanced photocatalytic activity [36-38]. EPR analysis was carried out to monitor reactive oxygen species. The measurement was performed at 293 K using 5,5-dimethyl-1-pyrroline N-oxide as the spin trapping agent. Fig. 5(a) and (b) display EPR spectra of aqueous solution of ZnO and AZNs under both dark condition and light irradiation It can be seen that there was no obvious signal in dark condition. However, four distinct signals belonging to DMPO-OH were observed under UV light irradiation and the intensity of signals became stronger with increasing Ag concentration. This reveals that the amount of $OH^-$ formed on the surface of AZNs is more than that of pristine ZnO [39,40]. To further study the photoelectrochemical performance, the photocurrents of ZnO and AZNs under UV light irradiation were measured. As shown in Fig. 6, AZNs generated more photocurrent than unmodified ZnO. This result indicates that AZNs tend to more easily generate charge carriers and separated electrons, which determines the photocatalytic efficiency. Therefore, AZNs are expected to perform enhanced photocatalytic activity [41,42].

**2. Photocatalytic Activity**

The photocatalytic mechanism of AZNs can be explained by the following equations [43,44]:

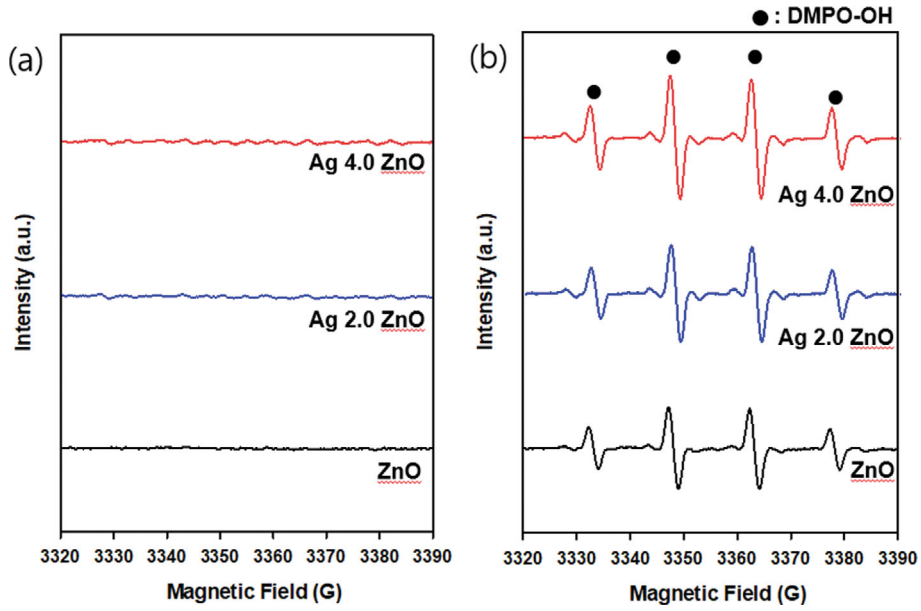


**Fig. 5. EPR analysis of ZnO, Ag 2.0 ZnO and Ag 4.0 ZnO under (a) dark condition and (b) UV irradiation.**

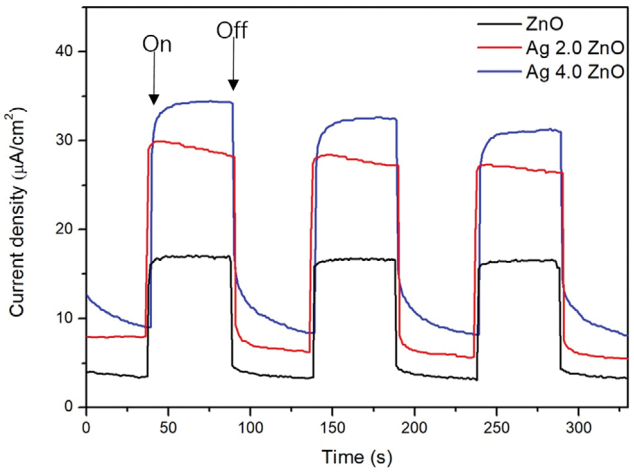


**Fig. 6. Photocurrent measurement of ZnO, Ag 2.0 ZnO and Ag 4.0 ZnO electrodes in 0.5 M phosphate buffer solution.**

$$Ag/ZnO+hv \rightarrow Ag/ZnO(e^-_{CB}+h^+_{VB}) \quad (2)$$

$$Ag/ZnO(h^+_{VB})+H_2O_{(ads)} \rightarrow Ag/ZnO+H^++OH^{\bullet} \quad (3)$$

$$Ag/ZnO(e^-_{CB})+O_{2(ads)} \rightarrow O_2^{\bullet-} \quad (4)$$

$$Ag^++e^-_{CB} \rightarrow Ag \quad (5)$$

$$O_2^{\bullet-}+H^+ \rightarrow HO_2^{\bullet} \quad (6)$$

$$OH^{\bullet}(\text{or } HO_2^{\bullet})+MB \rightarrow CO_2+H_2O \quad (7)$$

When Ag-doped ZnO semiconductor is irradiated by UV light and visible light with a photonic energy greater than band gap, an electron from the valence band (VB) is excited and transferred to a conduction band (CB) to produce an electron hole pair (Eq. (2)). Water or hydroxyl radicals react with holes in the valence band and produce hydroxyl radicals (Eq. (3)). The electrons in the conduction band react with $O_2$ to generate superoxide anion radicals (Eq. (4)). The Ag dopant accepts the photogenerated electron in the conduction band of ZnO (Eq. (5)). Thus, the photogenerated charge carriers can be easily separated to improve the photocatalytic activity under both UV and visible light irradiation. The photocatalytic mechanism of particles is described in Fig. 7(a). The hydrogen peroxide radicals formed by radical anion react with $H^+$ in water (Eq. (6)). The hydrogen peroxide radicals act as oxidizing agents to break down organic pollutants such as MB. In this study, the photocatalytic activity of synthesized nanoparticles was examined under UV as well as visible light. Fig. 7(b)-(d) shows the time-dependent absorption spectra of MB aqueous solution under UV irradiation with ZnO and AZNs. The efficiency of degradation was evaluated by using the following equation [45,46].

$$\text{MB degradation}=(C_0-C_t)/C_0 \quad (8)$$

where $C_0$ represents the initial concentration of MB and $C_t$ is the concentration after the irradiation of lights for time t.

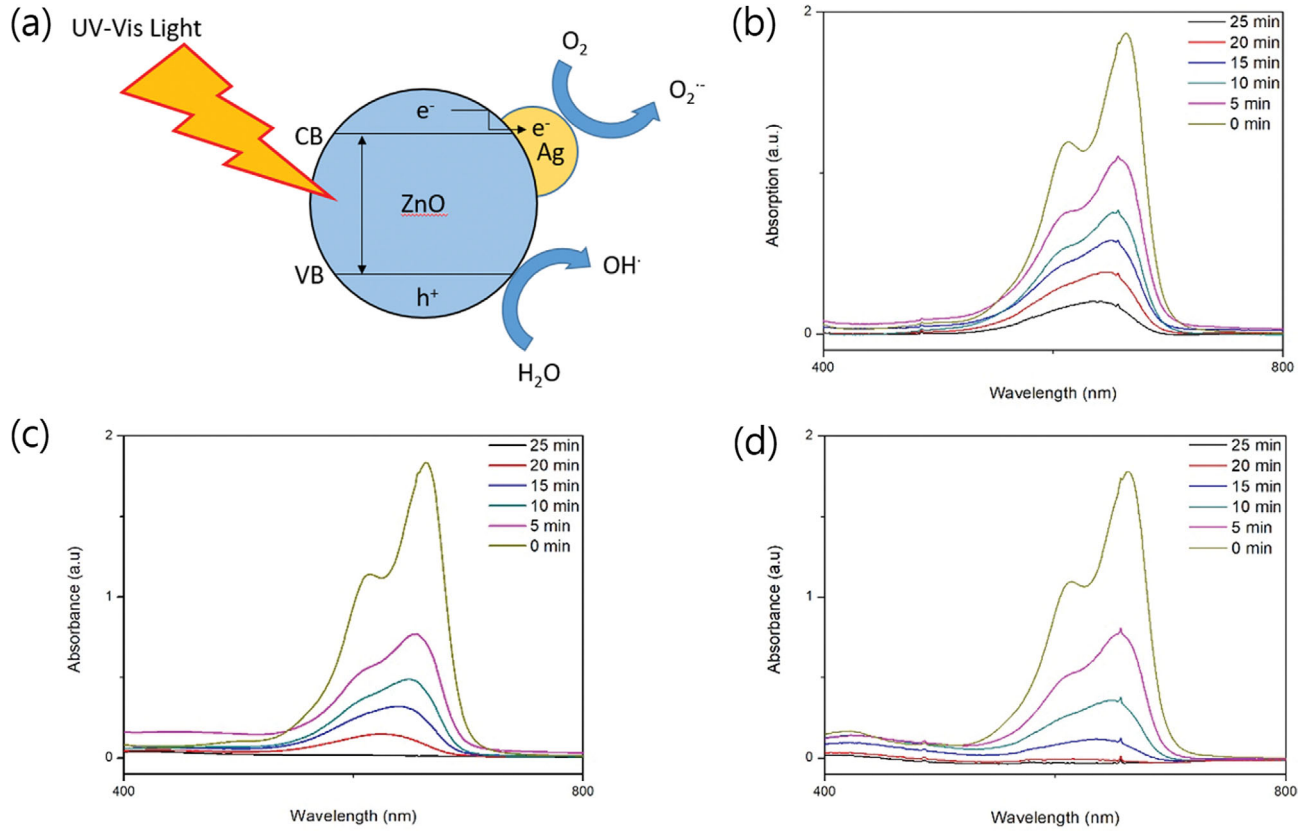


**Fig. 7. (a) Schematic diagram of photocatalysis mechanism of AZN and the absorption spectra of methylene blue after photocatalytic degradation by (b) ZnO, (c) Ag 2.0 ZnO and (d) Ag 4.0 ZnO.**

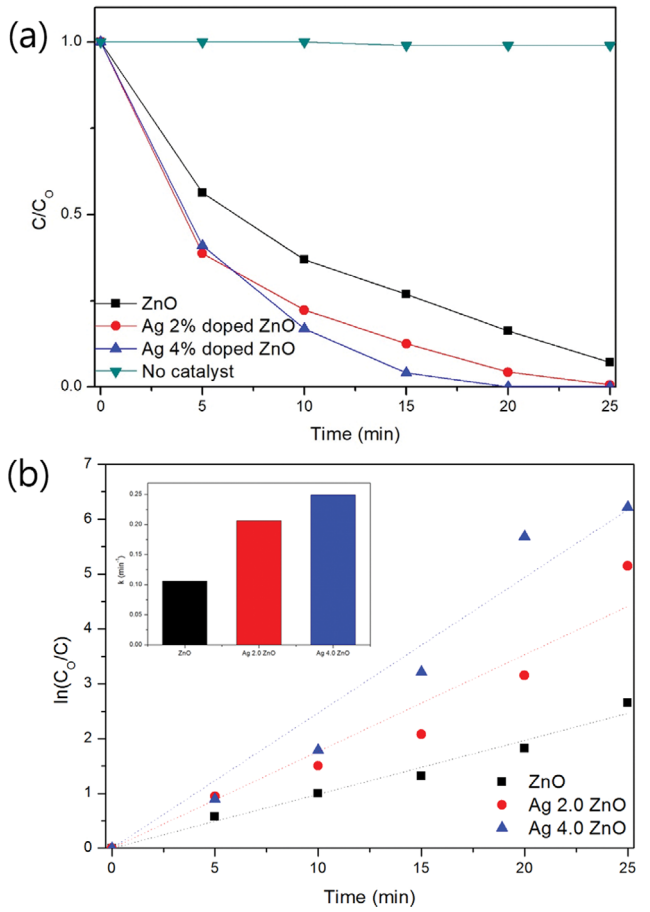


**Fig. 8. (a) Degradation of Methylene blue by ZnO, Ag 2.0 ZnO, and Ag 4.0 ZnO under UV light irradiation, and (b) corresponding pseudo-first-order plots used for the determination of the rate constants.**

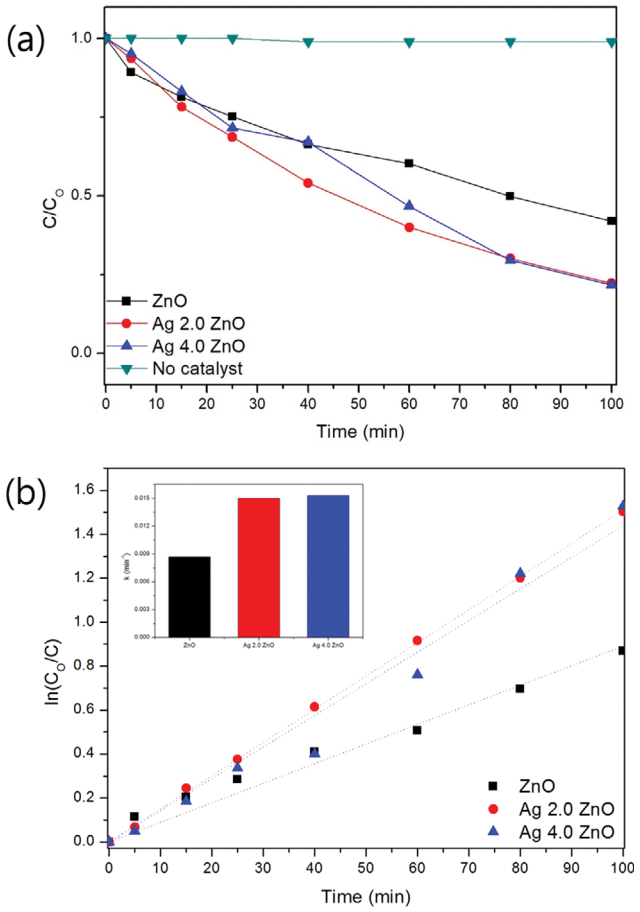


**Fig. 9. (a) Degradation of Methylene blue by ZnO, Ag 2.0 ZnO, and Ag 4.0 ZnO under visible light irradiation, and (b) corresponding pseudo-first-order plots used for the determination of the rate constants.**

Fig. 8(a) indicates that photocatalytic activity of AZNs samples was greater than that of pristine ZnO nanoparticles. The Ag 4.0 ZnO displayed the highest photocatalytic MB degrading performance: 96.0% degradation after 15 min and degraded fully in 20 min. The lowest photocatalytic activity was observed with pristine ZnO nanoparticles. The 92.9% photodegradation was observed within 25 min. In addition, the apparent quantum efficiency of ZnO, Ag 2.0 ZnO and Ag 4.0 ZnO under UV irradiation was calculated and found to be 0.873, 0.651, and 0.507%, respectively. The efficiency of photodegradation of MB under UV light was increased as the concentration of Ag increased in AZNs. The pseudo-first-order kinetics model was calculated using (Eq. (9)) and plotted in Fig. 8(b).

$$\ln\frac{C}{C_0} = kt \tag{9}$$

where, t represents the irradiation time and k is the pseudo-first-order rate constant. The values of the pseudo-first-order rate constant of ZnO, Ag 2.0 ZnO and Ag 4.0 ZnO was 0.106 $min^{-1}$, 0.206 $min^{-1}$ and 0.249 $min^{-1}$, respectively. The reaction rate constant for Ag 4.0 ZnO was 2.5 times higher than that of pristine ZnO. Fig. 9(a) shows the photodegradation of MB in the presence of ZnO and AZNs under visible light irradiation. It was observed that the photodegradation efficiency under visible light was also enhanced by Ag doping. The ZnO, Ag 2.0 ZnO and Ag 4.0 ZnO photocatalysts degraded 54.8, 77.7, and 78.3% of MB after 100 min irradiation, respectively. According to the calculated pseudo-first-order kinetic constant (Fig. 9(b)), the ZnO, Ag 2.0 ZnO and Ag 4.0 ZnO exhibited k values of 0.00869 $min^{-1}$, 0.0150 $min^{-1}$ and 0.0153 $min^{-1}$, respectively. Ag doped ZnO resulted in better photocatalytic degradation of MB under visible light than pristine ZnO. However, ZnO with higher dopant concentration showed similar photocatalytic activity to ZnO with lower dopant concentration. The photocatalytic efficiency of Ag 4.0 ZnO can be reduced by the accumulation of excess dopant on the surface, covering the surface and preventing light and MB molecules adsorption. Besides, it has been found that excessive defects could behave as recombinant center to promote photoexcited electron-hole pairs during photocatalysis [47,48]. The improvement of photocatalytic activity is related to the changes in electronic structure of ZnO by inserting Ag ions into Zn lattice. In consequence, the photoexcited electron hole pairs could be efficiently separated, resulting in improved photocatalytic performance [49,50].

### 3. Characterization of Nanofibers

PAN nanofibers containing ZnO, Ag 2.0 ZnO and Ag 4.0 ZnO

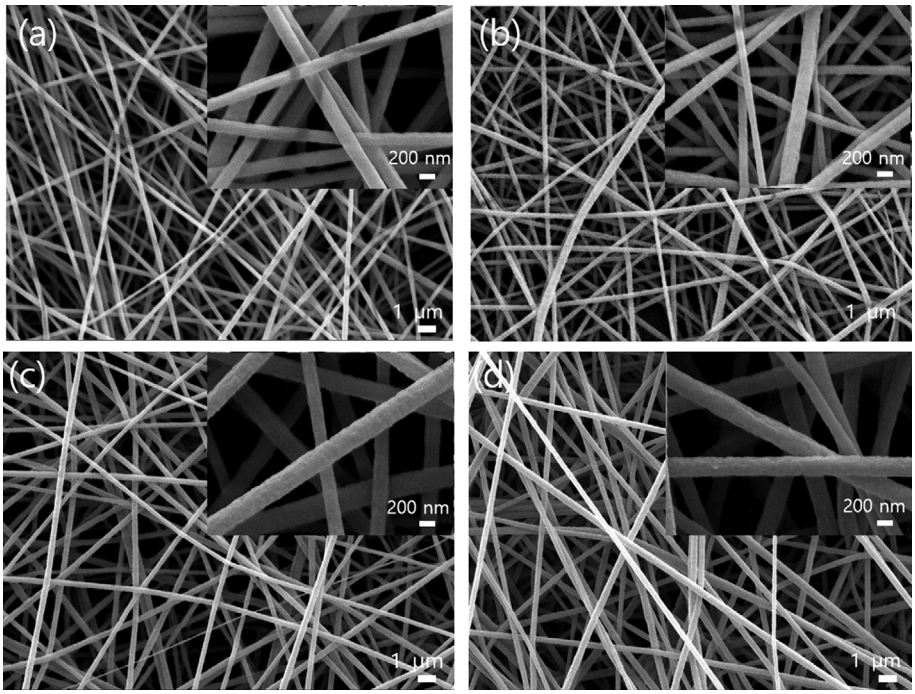


**Fig. 10. SEM images of (a) PAN, (b) ZnO/PAN, (c) Ag 2.0 ZnO/PAN, and (d) Ag 4.0 ZnO/PAN.**

**Table 1. EDS analysis results of PAN, ZnO/PAN, Ag 2.0 ZnO/PAN and Ag 4.0 ZnO/PAN**

| Samples | C (wt%) | O (wt%) | Zn (wt%) | Ag (wt%) |
|---|---|---|---|---|
| PAN | 93.66 | 6.34 | 0 | 0 |
| ZnO/PAN | 87.39 | 6.61 | 6.00 | 0 |
| Ag2.0ZnO/PAN | 86.26 | 7.59 | 5.90 | 0.25 |
| Ag4.0ZnO/PAN | 86.80 | 6.52 | 6.30 | 0.38 |

were fabricated by electrospinning technique, and they are denoted as ZnO/PAN, Ag 2.0 ZnO/PAN and Ag 4.0 ZnO/PAN. The SEM images of the electrospun nanofibers are shown in Fig. 10. The diameter of PAN nanofibers without ZnO nanoparticles was 272±50 nm, and average diameter of composite nanofibers was 319±35 nm, 343±57 nm, and 336±64 nm for ZnO/PAN, Ag 2.0 ZnO/PAN and Ag 4.0 ZnO/PAN, respectively. The PAN nanofibers with nanoparticles have larger diameters compared with that of bare PAN nanofibers, which can be attributed to the increase in viscosity by adding nanoparticles to the polymeric solution [51]. It is well known that the higher viscosity of electrospinning solution causes hindrance to flow of the solution jet toward collector, resulting in an increased diameter [52]. The presence of Ag-doped ZnO and pristine ZnO particles on nanofibers was confirmed by EDS analysis. The chemical composition of nanofibers is listed in Table 1. The results clearly indicate that the percentage of Ag increased as the used amount of Ag dopant increased. Also, Ag species were not detected for PAN and ZnO/PAN nanofibers. For further investigation, the FE-SEM image of Ag 4.0 ZnO/PAN nanofiber is shown in Fig. 11(a) and corresponding mapping images are shown in Fig. 11(b)-(d). The obtained mapping images indicate that Ag, Zn and O ions are uniformly distributed in the nanofiber. TEM analyses were conducted.

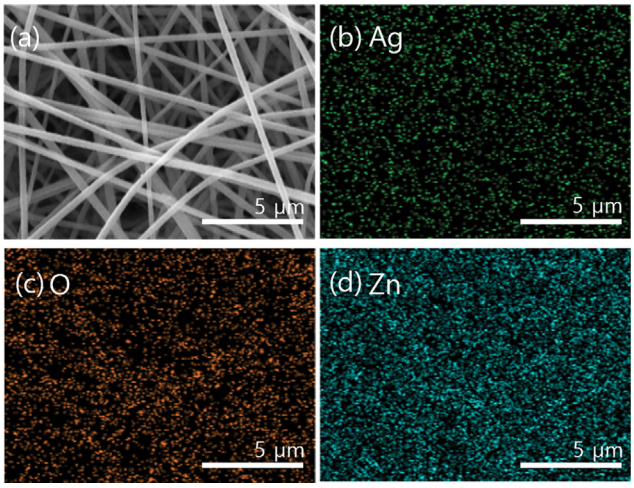


**Fig. 11. (a) SEM image of Ag 4.0 ZnO/PAN nanofiber and EDS mapping results for (b) silver, (c) oxygen and (d) zinc elements.**

After electrospinning, the fabricated nanofibers were ultrasonicated to separate individually, then loaded on TEM grid. Fig. 12(a) shows that the bare PAN nanofiber without ZnO nanoparticles appeared to be homogeneous and uniform. On the other hand, Ag-doped and pristine ZnO nanoparticles were observed inside and surface of electrospun composite nanofibers (Fig. 12(b)-(d)). It can be concluded that AZNs are successfully incorporated in PAN nanofiber and present on the surface of the fibers.

**4. Antiviral Activity**

The antiviral activity of fabricated nanofibers against model bacteriophage virus ($\phi$x174) was evaluated by monitoring the virus titers during the photocatalysis. In response to visible light irradia-

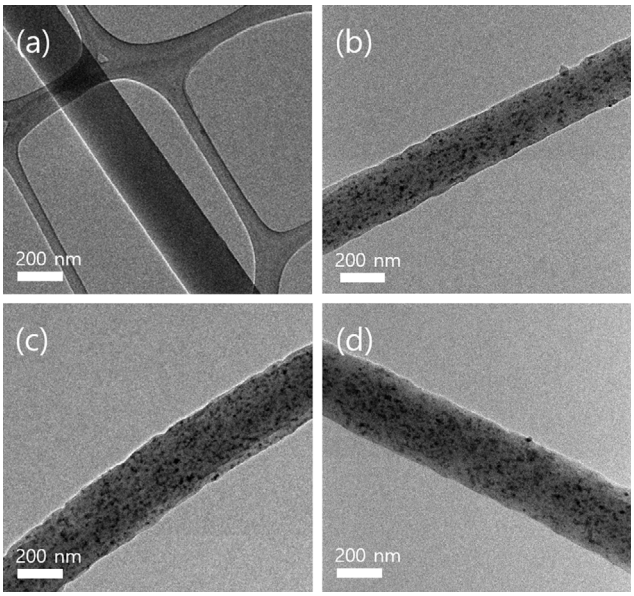


**Fig. 12. TEM images of (a) PAN, (b) ZnO/PAN, (c) Ag 2.0 ZnO/PAN, and (d) Ag 4.0 ZnO/PAN.**

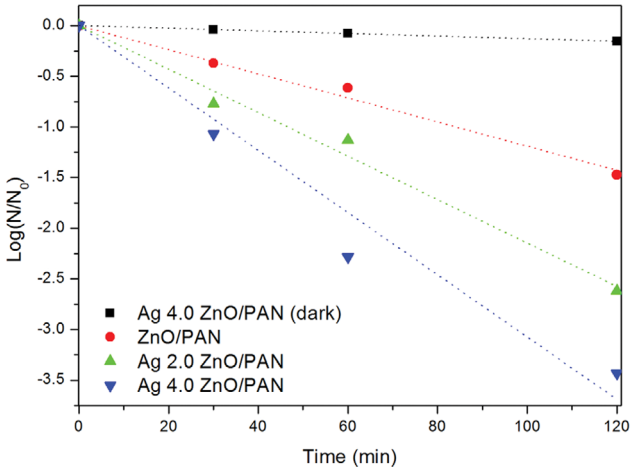


**Fig. 13. Antiviral activities of prepared nanofibers against $\phi$x174 under blue LED light ($\lambda$=470 nm) irradiations.**

tion, the reactive oxygen species, such as hydroxyl radical and superoxide, are created on the nanofiber with the AZNs, which oxidizes nearby viral envelopes and nucleic acids. As shown in Fig. 13, the titer of model viruses $\phi$x174 more rapidly decayed as the incorporated Ag content increased. The log reduction ($\log_{10}(N/N_0)$) in the $\phi$x174 titler of Ag 4.0 ZnO/PAN, Ag 2.0 ZnO/PAN and ZnO/PAN was −3.43, −2.62, and −1.47, respectively. Negligible antiviral activity of Ag 4.0 ZnO/PAN was observed under dark condition. This results clearly suggest that the physical contact with the ground state of ZnO compound in nanofibers is not a major contributor for antiviral activity.

The antiviral activity of Ag ions in ZnO could be related to its interaction with S-H group in cysteine residues of viral protein. Disulfide bond in cysteine and thiol group in cysteine residue are vital formations for protein to maintain the structure and function. The Ag ions inside and on the surface of AZNs react with thiol group in cysteine residue by replacing hydrogen atom to form R-S-Ag [53], which ends up with deteriorated enzymatic function of the protein. Moreover, disulfide bond in cysteine was obtained by the oxidation of two cysteine molecules cleaved by forming R-S-Ag according to the following reaction (Eq. (10)-(11)) [54].

$$R-SH+Ag^{+}\rightarrow R-S-Ag+H^{+} \quad (10)$$

$$R-S-S-R+Ag^{+}\rightarrow 2R-S-Ag \quad (11)$$

However, this reaction is not responsible for the enhancement of the Ag-induced inactivation of microorganism by visible light. It is clear that due to the photochemical reaction of the R-S-Ag complex, the ligand is oxidized and metallic Ag is formed as shown in Eq. (12).

$$R-S-Ag+hv\rightarrow R-S^{\bullet}+Ag \quad (12)$$

During light irradiation, Ag ions can obtain electrons from the chelated cysteine by ligand to metal charge transfer to produce metallic Ag and monosulfide radicals. The monosulfide radicals produced in cysteine of affected protein may react with other functional groups in viruses. Also, monosulfide radicals have a strong probability to oxidize other intracellular molecules by adsorbing hydrogen atoms [55]. Therefore, as the concentration of Ag dopant increases, more monosulfide radicals are formed under visible light, impairing more microbial functions and thus being inactivated.

## CONCLUSIONS

Ag-doped ZnO nanoparticles were successfully prepared via sol gel method, and synthesized particles were embedded into PAN nanofibers using electrospinning method. The AZNs have spherical shapes, and the size of nanoparticles was increased as the concentration of Ag in particles was increased. The band gap energy of AZNs was decreased as the concentration of Ag in ZnO nanoparticles was increased, resulting in slow recombination of electron-hole pairs. These results yielded outstanding photocatalytic performance of AZNs at high Ag concentration under the irradiation of UV and visible light. When the AZNs were embedded into PAN nanofibers, the diameters of nanofibers were slightly increased as the concentration of Ag in ZnO nanoparticles was increased. These results might be due to the larger particle size at high Ag concentration. Finally, according to inactivation test for bacteriophage $\phi$x174, the AZNs-containing nanofibers with the higher Ag content showed enhanced antiviral effect under visible light irradiation. Therefore, the photocatalytic activity of the synthesized AZNs is well correlated with their antiviral performance even incorporated in the electrospun nanofiber filter.

## ACKNOWLEDGEMENTS

This research was supported by Basic Science Research Program through the National Research Foundation of Korea (NRF) funded by the Ministry of Education (2016R1A6A1A03013422). This work was also supported by Samsung Research, Samsung Electronics Co., Ltd.

## REFERENCES


1. J. D. Cherry and P. Krogstad, *Pediatr. Res.*, **56**(1), 1 (2004).
2. M. P. Girard, J. S. Tam, O. M. Assossou and M. P. Kieny, *Vaccine*, **28**(31), 4895 (2010).
3. F. Jiang, L. Deng, L. Zhang, Y. Cai, C. Cheung and Z. Xia, *J. Gen. Intern. Med.*, **35**, 1545 (2020).
4. Z.-Y. Ge, L.-M. Yang, J.-J. Xia, X.-H. Fu and Y.-Z. Zhang, *J. Zhejiang Univ. Sci. B.*, **21**(5), 361 (2020).
5. J. L. Dembinski, O. Hungnes, A. G. Hauge, A. C. Kristoffersen, B. Haneberg and S. Mjaaland, *J. Virol. Methods*, **207**, 232 (2014).
6. W. R. Moorer, *Int. J. Dent Hyg.*, **1**(3), 138 (2003).
7. J.-H. Yoo, *J. Infect. Chemother.*, **50**(2), 101 (2018).
8. R. Fateh, R. Dillert and D. Bahnemann, *ACS Appl. Mat. Interfaces*, **6**(4), 2270 (2014).
9. J. Yoon and S.-G. Oh, *J. Ind. Eng. Chem.*, **96**, 390 (2021).
10. S.-E. Jin and H.-E. Jin, *Nanomaterials*, **11**(2), 263 (2021).
11. R. Nakano, H. Ishiguro, Y. Yao, J. Kajioka, A. Fujishima, K. Sunada, M. Minoshima, K. Hashimoto and Y. Kubota, *Photochem. Photobiol. Sci.*, **11**(8), 1293 (2012).
12. G. K. Upadhyay, J. K. Rajput, T. K. Pathak, V. Kumar and L. P. Purohit, *Vacuum*, **160**, 154 (2019).
13. J. Jiang, J. Pi and J. Cai, *Bioinorg. Chem. Appl.*, **2018**, 1062562 (2018).
14. R. Verma, S. Pathak, A. K. Srivastava, S. Prawer and S. Tomljenovic-Hanic, *J. Alloys Compd.*, **876**, 160175 (2021).
15. A. Kubiak, K. Siwińska-Ciesielczyk, Z. Bielan, A. Zielińska-Jurek and T. Jesionowski, *Adsorption*, **25**(3), 309 (2019).
16. M. Humayun, F. Raziq, A. Khan and W. Luo, *Green Chem. Lett. Rev.*, **11**(2), 86 (2018).
17. A. K. Chandiran, M. Abdi-Jalebi, M. K. Nazeeruddin and M. Grätzel, *ACS Nano.*, **8**(3), 2261 (2014).
18. R. Raji and K. G. Gopchandran, *J. Sci-Adv. Mater. Dev.*, **2**(1), 51 (2017).
19. M. Ilka, S. Bera and S.-H. Kwon, *Materials*, **11**(6), 904 (2018).
20. S. Fabbiyola, L. J. Kennedy, U. Aruldoss, M. Bououdina, A. A. Dakhel and J. JudithVijaya, *Powder Technol.*, **286**, 757 (2015).
21. Y. Wang, Y. Yang, X. Zhang, X. Liu and A. Nakamura, *CrystEngComm.*, **14**(1), 240 (2012).
22. N. Ali, B. Singh, Z. A. Khan, V. A. R, K. Tarafder and S. Ghosh, *Sci. Rep.*, **9**(1), 2461 (2019).
23. H. B. Dias, M. I. B. Bernardi, V. S. Marangoni, A. C. de Abreu Bernardi, A. N. de Souza Rastelli and A. C. Hernandes, *Mater. Sci. Eng. C.*, **96**, 391 (2019).
24. W. L. Ong, H. Huang, J. Xiao, K. Zeng and G. W. Ho, *Nanoscale*, **6**(3), 1680 (2014).
25. A. Naskar, S. Lee and K.-s. Kim, *RSC Adv.*, **10**(3), 1232 (2020).
26. S. S. Jeremiah, K. Miyakawa, T. Morita, Y. Yamaoka and A. Ryo, *Biochem. Biophys. Res. Commun.*, **533**(1), 195 (2020).
27. A. Di Mauro, M. Zimbone, M. E. Fragalà and G. Impellizzeri, *Mater. Sci. Semicond. Process.*, **42**, 98 (2016).
28. K. Roongraung, S. Chuangchote, N. Laosiripojana and T. Sagawa, *ACS Omega.*, **5**(11), 5862 (2020).
29. J.-H. Kim, J.-H. Lee, J.-Y. Kim and S. S. Kim, *Appl. Sci.*, **8**(2), 309 (2018).
30. Q.-Y. Wu, L.-S. Wan and Z.-K. Xu, *J. Membr. Sci.*, **409-410**, 355 (2012).
31. D. Yadav, F. Amini and A. Ehrmann, *Eur. Polym. J.*, **138**, 109963 (2020).
32. A. D. Eaton, *Standard methods for the examination of water and wastewater*, American Public Health Association, Washington D.C. (2005).
33. M. Silambarasan, S. Shanmugam and T. Soga, *Int. J. ChemTech. Res.*, **7**, 1644 (2015).
34. E. S. Nour, A. Echresh, X. Liu, E. Broitman, M. Willander and O. Nur, *AIP Adv.*, **5**(7), 077163 (2015).
35. S. Kumar, V. Singh and A. Tanwar, *J. Mater. Sci. Mater. Electron.*, **27**(2), 2166 (2016).
36. F. Hosseini, A. Kasaeian, F. Pourfayaz, M. Sheikhpour and D. Wen, *Mater. Sci. Semicond. Process.*, **83**, 175 (2018).
37. Y. Jerlin Jose, M. Manjunathan and S. Joseph Selvaraj, *J. Nanostructure. Chem.*, **7**(3), 259 (2017).
38. L. Wang, *Int. J. Electrochem. Sci.*, **14**, 9150 (2019).
39. J. Peng, T. Lu, H. Ming, Z. Dingm Z. Yu J. Zhang and Y. Hou, *Catalysts*, **9**(12), 1006 (2019).
40. J. Li, M. Zhou, Z. Ye, H. Wang, C. Ma, P. Huo and Y. Yan, *RSC Adv.*, **5**(111), 91177 (2015).
41. B. Seitov, S. Kurbanbekov, D. Bakarnova, N. Abdyldayeva and N. Bakranov, *Catalysts*, **11**(10), 1235 (2021).
42. Y. Yu, *Int. J. Electrochem. Sci.*, **16**, 210259 (2021).
43. O. Bechambi, M. Chalbi, W. Najjar and S. Sayadi, *Appl. Surf. Sci.*, **347**, 414 (2015).
44. Z. Zhang, H. Liu, H. Zhang H. Dong, X. Liu, H. Jia and B. Xu, *Superlattices Microstruct.*, **65**, 134 (2014).
45. K. Saoud, R. Al-Soubaih, S. Saeed, N. Bensalah, M. Al-Fandi and T. Singh, *J. Mater. Environ. Sci.*, **9**, 400 (2018).
46. M. Ahmad, I. Ahmad, E. Ahmed, M. S. Akhtar and N. R. Khalid, *J. Mol. Liq.*, **311**, 113326 (2020).
47. M. Cardoza-contreras, A. Vasquez-gallegos, A. Vidal-Limon, J. Romoherrera, S. Aguila and O. Contreras, *Catalysts*, **9**(2), 165 (2019).
48. H. Liu G. Shao, J. Zhao, Z. Zhang, J. Liang, X. Liu, H. Jia and B. Xu, *J. Phys. Chem. C.*, **116**(30), 16182 (2012).
49. F. A. Alharthi, A. A. Alghamdi, N. Al-Zaqri, H. S. Alanazim A. A. Alsyahi, A. E. Marghany and N. Ahmad, *Sci. Rep.*, **10**(1), 20229 (2020).
50. L. Zhang, X. Zhu, Z. Wang, S. Yun, T. Guo, J. Zhang, T. Hu, J. Jiang and J. Chen, *RSC Adv.*, **9**(8), 4422 (2019).
51. J. Kim, T. Kang, H. Kim, H. J. Shin and S.-G. Oh, *J. Ind. Eng. Chem.*, **77**, 273 (2019).
52. T. Pirzada, S. A. Arvidson, C. D. Saquing, S. S. Shah and S. A. Khan, *Langmuir*, **28**(13), 5834 (2012).
53. M. Minoshima, Y. Lu, T. Kimura, R. Nakano, H. Ishiguro, Y. Kubota, K. Hashimoto and K. Sunada, *J. Hazard. Mater.*, **312**, 1 (2016).
54. K. Siriwardana, A. Wang, M. Gadogbe, W. E. Collier, N. C. Fitzkee and D. Zhang. *J. Phys. Chem. C.*, **119**(5), 2910 (2015).
55. J. Y. Kim, C. Lee, M. Cho and J. Yoon, *Water Res.*, **42**(1), 356 (2008).